Prompt neutron polarization asymmetries in photofission of ²³²Th, ²³³,²³⁵,²³⁸U, ²³⁷Np, and ²³⁹,²⁴⁰Pu

J. M. Mueller,[1,2] M. W. Ahmed,[1,2,3] R. H. France, III,[4] M. S. Johnson,[5,6] H. J. Karwowski,[1,7] L. S. Myers,[1,2,*]
J. Randrup,[8] M. H. Sikora,[1,9] M. C. Spraker,[10] S. Stave,[11] J. R. Tompkins,[1,7,†] R. Vogt,[5,12] H. R. Weller,[1,2]
C. S. Whisnant,[13] and W. R. Zimmerman[1,2,14]

[1]*Triangle Universities Nuclear Laboratory, Durham, North Carolina 27708, USA*
[2]*Department of Physics, Duke University, Durham, North Carolina 27708, USA*
[3]*Department of Mathematics and Physics, North Carolina Central University, Durham, North Carolina 27707, USA*
[4]*Department of Chemistry, Physics, and Astronomy, Georgia College and State University, Milledgeville, Georgia 31061, USA*
[5]*Physics Division, Lawrence Livermore National Laboratory, Livermore, California 94551, USA*
[6]*Department of Physics and Astronomy, San Jose State University, San Jose, California 95192, USA*
[7]*Department of Physics and Astronomy, University of North Carolina–Chapel Hill, Chapel Hill, North Carolina 27599, USA*
[8]*Nuclear Science Division, Lawrence Berkeley National Laboratory, Berkeley, California 94720, USA*
[9]*Department of Physics, George Washington University, Washington, DC 20052, USA*
[10]*Department of Physics, University of North Georgia, Dahlonega, Georgia 30597, USA*
[11]*Pacific Northwest National Laboratory, Richland, Washington 99352, USA*
[12]*Department of Physics, University of California–Davis, Davis, California 95616, USA*
[13]*Department of Physics, James Madison University, Harrisonburg, Virginia 22807, USA*
[14]*Department of Physics, University of Connecticut–Storrs, Storrs, Connecticut 06269, USA*
(Received 13 January 2014; published 19 March 2014)

Photofission experiments were performed on targets of ²³²Th, ²³³,²³⁵,²³⁸U, ²³⁷Np, and ²³⁹,²⁴⁰Pu using nearly 100% linearly polarized, high intensity ($\sim 5 \times 10^6 \gamma$/s), and nearly-monoenergetic γ-ray beams having energies between 5.3 and 7.6 MeV at the High Intensity γ-ray Source (HIγS) located at Duke University and Triangle Universities Nuclear Laboratory. An array of 12–18 liquid scintillator detectors was used to measure prompt fission neutron yields parallel and perpendicular to the plane of beam polarization. Polarization asymmetries, the differences between the in-plane and out-of-plane yields divided by their sums, were measured. Asymmetries close to zero were found for ²³³,²³⁵U, ²³⁷Np, and ²³⁹Pu while significant asymmetries ($\sim$0.2–0.5) were found for ²³²Th, ²³⁸U, and ²⁴⁰Pu. Predictions based on previously measured photofission fragment angular distributions combined with a model of prompt neutron emission agree well with the experimental results.

PACS number(s): 25.85.Jg, 24.70.+s, 24.75.+i, 25.20.−x

I. INTRODUCTION

Prompt neutrons are a key component of the fission process. It has been well established that the majority of the prompt neutrons are emitted after the fragments are nearly fully accelerated and thus are correlated in emission angle with the fission fragments [1]. Measurements of photofission fragment angular distributions for beam energies between 5 and 7 MeV have shown significant anisotropies relative to the beam direction in the case of photofission of even-even actinides [2] and nearly isotropic angular distributions for odd-*A* actinides [3–5]. Due to the angular correlation between the prompt neutrons and the fission fragments, the anisotropy in the fission fragments for even-even photofission should be detectable in the angular distribution of the prompt neutrons. Therefore, the prompt neutron angular distribution can serve as a high-precision probe of the underlying fission fragment angular distribution, which can be difficult to measure at a high precision due to the angular straggling of fragments in the

target. Our work shows that measured prompt neutron angular distributions and polarization asymmetries can be understood in terms of underlying fission fragment angular distributions combined with a model of prompt neutron emission. This serves as an extension of our previous work [6].

Section II summarizes previous work done to measure and understand angular distributions in photofission between 5 and 7 MeV and discusses previous studies of the emission of neutrons from the excited fission fragments. Section III discusses our experiments to measure prompt neutron polarization asymmetries, and Sec. IV describes the analysis procedure to extract the prompt neutron polarization asymmetries and angular distribution coefficients. Section V shows our experimental results, and Sec. VI describes the prompt neutron emission model and compares its results to the experimental results. More details regarding any specific section and tabulated results can be found in Ref. [7].

II. PREVIOUS WORK ON ANGULAR DISTRIBUTIONS IN PHOTOFISSION

A. Previous measurements of angular distributions in photofission

Many measurements of angular distributions in photofission using γ rays between 5 and 7 MeV have been performed.

Most of these experiments investigated the fission fragment angular distributions with unpolarized, bremsstrahlung beams [2,3,5,8–17]. Some of these works have attempted to reconstruct the angular distribution as a function of monoenergetic γ-ray quanta [2,3,16], which makes them suitable for comparison with quasi-monoenergetic beam results, such as ours. Typically, the reconstructed angular distributions are presented without uncertainties. Fewer experiments have directly used unpolarized, quasi-monoenergetic beams to measure fragment angular distributions [4,10,18–20]. Still fewer experiments have used linearly polarized beams to measure fragment angular distributions [21–24]. Linearly polarized beams enhance the sensitivity of measurements of angular distributions coefficients. Except for a previous publication on a subset of the present results [6], only one previous measurement of prompt neutron angular distributions in photofission has been reported; it employed an unpolarized, bremsstrahlung beam to induce photofission of ^{232}Th and ^{238}U [25].

Historically, the angular distributions have been reported in the form $W(\theta) = a + b\sin^2\theta + c\sin^2 2\theta$, where θ is the angle between the fission fragment and the beam direction [2]. The normalization $a + b = 1$ is typically used. Here the b coefficient will be referred to as the anisotropic dipole coefficient, and the c coefficient as the quadrupole coefficient. In general, the photofission fragment angular distributions have shown large dipole anisotropies for the even-even actinides, as shown in Fig. 1. Anisotropic dipole photofission dominates in ^{232}Th until approximately 6.5 MeV, when the angular distribution becomes more isotropic. Anisotropic dipole photofission also dominates photofission of ^{238}U and ^{240}Pu until approximately 6 and 5.5 MeV, respectively. ^{238}U and ^{240}Pu both show

significant quadrupole contributions to photofission at beam energies near 5 MeV, though ^{232}Th does not [2].

Photofission fragment measurements of odd-A actinides show much more isotropic angular distributions. Of the odd-A actinides, ^{239}Pu has the largest anisotropic dipole contribution, though it is still significantly smaller than that of ^{232}Th and ^{238}U [3]. ^{237}Np has been measured with monoenergetic beams, and small anisotropies were observed [4]. Bremsstrahlung measurements on ^{233,235}U show angular distributions consistent with isotropy [5,12].

B. Photofission angular distribution theory

After some of the early data on photofission fragment angular distributions were published [17], a model was developed to explain the anisotropies found in the photofission of even-even nuclei [26]. This model, termed the photofission channel formalism, relates the fragment angular distribution to the excitation spectrum of the highly deformed saddle-point nucleus. Each excited saddle-point state has a total angular momentum value J and an angular momentum projection along the symmetry axis K. The J and K quantum numbers specify the orientation of the deformed nucleus at the saddle point of the outer barrier. The fission should proceed quickly enough that K does not change in the descent from saddle to scission. It is generally assumed that the direction of the symmetry axis directly gives the direction of motion of the two fission fragments [26], though this violates the uncertainty principle because it implies an infinite uncertainty in the angular momentum of the fissioning nucleus [27–29]. However, the corrections to the angular distributions predicted by reasonable uncertainties of angular momenta are small enough to be neglected in the present case [28].

For beam energies approaching the photofission threshold, the saddle-point nucleus is assumed to be thermodynamically cold and only a few excited states are energetically accessible. Fission proceeding through one of these states will induce a specific angular distribution in the fission fragments, depending on the J and K values of the state, and the angular distributions will generally be different for different values of J and K. If one of these states is more populated than the others or if their probability of penetrating the fission barrier is very different, the resulting fragment angular distribution can become very anisotropic. For beam energies of several MeV above the photofission threshold, more states are energetically available. When these states are equally populated, the superposition of contributions from all of these individual states leads to an isotropic fragment angular distribution.

This model can qualitatively account for much of the experimental data on fragment angular distributions. At low excitation energies, the model predicts large dipole anisotropies in the even-even actinides. The $(J^\pi, K) = (1^-, 0)$ state, corresponding to a mass asymmetric vibration, is expected to be at a lower excitation energy at the outer barrier than the $(1^-, \pm 1)$ states, which correspond to a bending vibration [1]. The angular distribution from the $(1^-, 0)$ state in the channel formalism is $\frac{3}{4}\sin^2\theta$, while the angular distribution from the $(1^-, \pm 1)$ states is $\frac{3}{4} - \frac{3}{8}\sin^2\theta$. At low beam energies
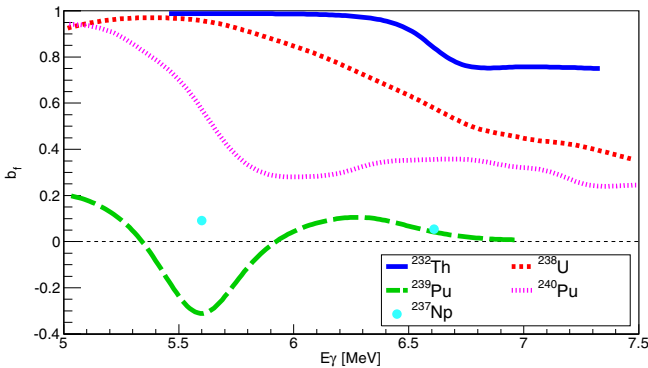

FIG. 1. (Color online) Previous measurements of fragment angular distributions. The angular distribution was parametrized as $W(\theta) = a_f + b_f \sin^2\theta$, where the f subscript indicates a fragment angular distribution, and the normalization $a_f + b_f = 1$ was chosen. The data on ^{232}Th, ^{238}U, and ^{240}Pu are from Ref. [2], while the data on ^{239}Pu are from Ref. [3]. The data on these isotopes are from bremsstrahlung measurements that have been reconstructed to approximate quasi-monoenergetic γ-ray beams, and are not presented with any uncertainties. The data on ^{237}Np is from Ref. [4], which used a monoenergetic beam. The uncertainties from Ref. [4] are smaller than the size of the data points.

($\sim$5 MeV), the (1^-,0) state should be preferentially populated, leading to positive values of b_f and values of a_f close to 0; under the normalization $a_f + b_f = 1$, b_f would tend to 1. As the beam energy increases, the population of the (1^-, ± 1) states should increase, leading to values of b_f closer to 0. This is in qualitative agreement with observations summarized in Fig. 1. The channel formalism also predicts significant quadrupole anisotropies in ^{238}U and ^{240}Pu, but not ^{232}Th, in accordance with the experimental results. In the model, this phenomenon occurs because the inner barrier is higher than the outer barrier in ^{238}U and ^{240}Pu but not in ^{232}Th, and the reflection symmetry at the outer barrier and inner barrier is different [1].

Finally, the model can also account for the more isotropic fragment angular distributions from photofission of odd-A actinides. Because the odd-A nuclei have a randomly oriented $J \neq 0$, any observed anisotropy due to the absorption of a photon with spin 1 will be diminished relative to the case of an even-even nucleus with $J = 0$ [30]. In addition, the level density at the saddle point near the photofission threshold of an odd-A nucleus should be higher than for an even-even nucleus [4]. Due to the higher number of open fission channels in odd-A nuclei compared to even-even nuclei, the resulting fragment angular distribution should be more isotropic.

C. Parameterization of angular distributions and polarization asymmetries in photofission

Using the formalism of Ref. [1] and assuming only electric dipole and quadrupole photofission with no interference terms, the relative fragment or neutron yield as a function of polar angle (θ) can be parametrized as

$$W(\theta) = a + b \sin^2 \theta + c \sin^2 2\theta, \qquad (1)$$

Using these same assumptions, the angular distribution resulting from a linearly polarized beam induced reaction can be obtained by using Racah techniques [31] augmented by the concept of statistical tensors [32]. This procedure was applied in Ref. [33] for the case of linearly polarized γ-ray beams and results in a $\cos 2\phi$ dependence as discussed by Ref. [34], where ϕ is the azimuthal angle of the outgoing particle relative to the plane of beam polarization. The prescription for translating the angular distribution using an unpolarized beam to a linearly polarized beam can also be found in Refs. [35,36] along with all coupling coefficients needed for different multipolarities. In our work it is assumed that there is no contribution from quadrupole channels with $K = 1$ or 2, since those channels are not likely to contribute to the fission process due to their high predicted energies at the saddle point [1]. The polarized angular distribution is

$$\begin{aligned} W(\theta,\phi) = {} & a + b \sin^2 \theta + c \sin^2 2\theta \\ & + P_\gamma \cos 2\phi (b \sin^2 \theta + c \sin^2 2\theta), \qquad (2) \end{aligned}$$

where P_γ is the fractional beam polarization, which is taken to be 1.0 in the present case. The a and b coefficients are normalized such that $a + b = 1$. Any anisotropy in the unpolarized angular distribution leads to anisotropy in ϕ when using a linearly polarized beam.

The polarization asymmetry $\Sigma(\theta)$ is given in terms of the yields at different angles ϕ by

$$\Sigma(\theta) = \frac{W(\theta,0^\circ) + W(\theta,180^\circ) - W(\theta,90^\circ) - W(\theta,270^\circ)}{W(\theta,0^\circ) + W(\theta,180^\circ) + W(\theta,90^\circ) + W(\theta,270^\circ)}. \qquad (3)$$

Using Eq. (2) and the normalization $a + b = 1$, this reduces to

$$\Sigma(\theta) = \frac{b \sin^2 \theta + c \sin^2 2\theta}{1 - b + b \sin^2 \theta + c \sin^2 2\theta}. \qquad (4)$$

D. Neutrons generated from fission

Prompt neutrons make up the majority ($\sim 95\%$) of the neutron yield from fission [37,38]. They are well described by an evaporation process and are therefore assumed to be emitted with no preferred direction in the rest frame of the fragment [39], although theoretical calculations indicate that a small anisotropy of the neutron angular distribution in the rest frame of the fragment may exist [40–42]. The contribution of the small anisotropy may be a few percent of the magnitude of the isotropic component [42]. The prompt neutrons are expected to be emitted by nearly fully accelerated fragments [39], so a correlation is expected between the photofission neutron angular distribution and the fragment angular distribution. This correlation has been confirmed by the measurements of Ref. [25] for near-threshold photofission of ^{238}U and ^{232}Th using an unpolarized beam. In these measurements, the neutron angular distributions were anisotropic but significantly less anisotropic than the fragment angular distributions. This implies that if a linearly polarized beam is used to induce photofission, neutron polarization asymmetries may be measurable but should be smaller in magnitude than any fragment polarization asymmetries. Our early data confirmed this assumption [6].

III. EXPERIMENT DESCRIPTION

A. Beam and target information

The High Intensity γ-ray Source (HIγS), located at Duke University and Triangle Universities Nuclear Laboratory, generated the γ-ray beams for this experiment. The HIγS facility is a quasi-monoenergetic Compton γ-ray source with a wide energy range and switchable linear and circular polarizations. The facility has been described in detail elsewhere [43–45], therefore only a short description is provided here. A nearly-monoenergetic, high-flux γ-ray beam is created by colliding a two-bunch electron beam in a storage ring with a high-power intracavity free-electron laser (FEL) beam. For this experiment, the FEL wavelength was $\sim$540 nm and the electron beam energies were selected to produce γ-ray beams between 5.30 and 7.60 MeV, with an energy spread (FWHM) of $\sim$ 3% at each beam energy. The γ-ray beams were produced having either $\sim$100% circular or linear polarizations. The γ-ray beam is pulsed with a period of 179 ns due to the duty factor of the electron storage ring, and the duration of each pulse ranged from 200 to 300 ps. The temporal structure of the γ-ray beam made it possible to use the time-of-flight method to

TABLE I. Masses and enrichments of the actinide targets.

Target	Mass (g)	Enrichment (%)	Main impurity
^{232}Th	17.36	99.9	
^{233}U	4.08	>97.5	^{232}Th (<2.5%)
^{235}U	4.62	93.7	^{238}U (6.3%)
^{238}U	6.88	99.1	
^{237}Np	4.40	99.9	
^{239}Pu	3.81	94.0	^{240}Pu (5.8%)
^{240}Pu	4.71	98.7	^{239}Pu (0.5%)

determine the energies of the detected neutrons. The absolute γ-ray intensity was measured using a large NaI detector, which was periodically moved into the beam following the insertion of a set of precision Cu attenuators. The measured unattenuated intensity, which was typically $\sim 5 \times 10^6$ γ/s, was continuously monitored with an array of five plastic scintillating paddles as described in Ref. [46]. The five-paddle array was calibrated to the intensity measurements from the large NaI detector.

Table I gives the masses and enrichments of the seven actinide targets used in the present work. All of the actinide targets were very highly enriched. Only a lower limit on the enrichment of the ^{233}U target could be determined by passive γ-ray counting due to the long half-life of ^{232}Th. Therefore, we are relying on an upper estimate of the amount of ^{232}Th contamination in the ^{233}U target which was provided by the scientist who performed the assay [47]. For the purposes of this paper, the enrichment of the ^{233}U target was assumed to be 97.5%.

The geometries of the targets varied significantly. The ^{232}Th and ^{235,238}U targets were foil targets which had no metal casing. The ^{233}U, ^{237}Np, and ^{239}Pu targets used a "lollipop" design, where the actinide material was in a small chamber in the center of a steel casing. Thin aluminum entrance and exit windows minimized the beam attenuation through the casing. The ^{240}Pu target was sealed in a chamber with thick aluminum walls. This led to significant neutron backgrounds through the ^{27}Al(α,n) reaction, where the ^{240}Pu sample was the source of the α particles. Estimated backgrounds due to this reaction were subtracted using out-of-time cuts as described in Sec. IV.

B. Detector array and electronics

An array of twelve to eighteen detectors was used to count neutrons generated by photofission. The active volume in each detector was filled with BC-501A liquid scintillator and was 12.7 cm in diameter and 5.1 cm thick. For most of the experiments performed, twelve detectors were placed at $\theta = 55°, 90°$, and $125°$, and at $\phi = 0°, 90°, 180°$, and $270°$, and the remaining six detectors were placed at $\theta = 72°, 107°$, and $142°$, and at $\phi = 0°$ and $90°$. In some cases not all detectors were available, so fewer detectors were used. In all cases, the target was positioned at the center of the detector array, and the flight path from the target to the detector was approximately 57 cm. A schematic diagram of the detector array is shown in Fig. 2.

The electronic circuit used to process the detector signals was built using Mesytec MPD-4 modules and analog electron-

FIG. 2. (Color online) A schematic of the detector array with all eighteen detectors, reproduced from Ref. [6]. The detectors are located at scattering angles of $\theta = 55°, 72°, 90°, 107°, 125°$, and $142°$.

ics [48]. The MPD-4 module used a detector signal as an input and returned separate signals containing the pulse height (PH), pulse-shape discrimination (PSD), and a trigger for each event that exceeded a threshold PSD value. The PSD value was used to discriminate against photon-like events. Digitization of the MPD-4 outputs was performed by analog-to-digital converters (ADCs) and the triggers were used to measure the time of flight (TOF) using time-to-digital converters (TDCs).

C. Detector calibration

The PH was calibrated using a ^{137}Cs source. Due to the finite resolution of the detector and multiple scattering effects [49], the 662 keV γ ray from the decay of ^{137}Cs appears as a Compton edge having a midpoint PH of 517 keV electron equivalent. The software detector thresholds are set relative to this leading edge in fractional increments, such as $\frac{1}{2} \times$Cs. The hardware PH threshold on the MPD-4 module was set below the software PH threshold. Because of its importance in determining software PH thresholds, multiple ^{137}Cs source runs were taken each day to monitor any potential gain drifts in the detectors. No gain drifts greater than one percent were observed. Source runs were also taken using an AmBe source, which is a combination γ-ray and neutron emitter, to adjust the MPD-4 PSD threshold settings to discriminate γ rays from neutrons. The PSD settings were checked twice daily with the AmBe source. Well known cable delays were used to calibrate the TDCs and determine the appropriate conversion from TDC values into nanoseconds.

D. Data collection

In addition to taking data on the actinide targets, data were taken using a D$_2$O target as an experimental confirmation of the time-of-flight method used in this experiment. An accurate energy calibration of the detectors was achieved

using the D_2O target because the energy of the neutron emitted upon photodisintegration of a deuteron depends only on the beam energy and emission angle. After finishing the energy calibration, an actinide target was mounted into the beam. Data were then taken using a circularly polarized beam for each actinide target to obtain correction factors for instrumental asymmetries. These instrumental effects, such as small differences in solid angle or efficiency between detectors in and out of the plane of beam polarization, could affect the measured polarization asymmetry of the prompt neutrons. The true polarization asymmetry when using a circularly polarized beam is exactly zero, so any observed asymmetries are instrumental. Because the prompt neutron spectrum should remain relatively unchanged over the range of γ-ray beam energies (5.3–7.6 MeV), only one beam energy (typically 7.0 MeV) was used to correct for instrumental asymmetries. After this correction was measured, a linearly polarized beam was used at a variety of beam energies for each of the seven actinide targets.

IV. DATA REDUCTION AND ANALYSIS

Several cuts were applied to the data to extract the neutron yields in each detector. The first cut applied to the data was a software PH cut. This cut ranged from $\frac{1}{4}\times$Cs to $\frac{1}{2}\times$Cs, or neutrons of approximately 1.0 to 1.5 MeV, depending on the detector voltage and the amount of electronic noise in the detector. The next cut applied was a two-dimensional PH-PSD cut. This cut was set using the AmBe source, and was intentionally kept loose around the neutrons. The main purpose of this cut was to eliminate a significant portion of the photon-like events. After this cut, a two-dimensional PSD-TOF cut was applied. This cut, shown in Fig. 3, attempted to remove the remaining γ-ray backgrounds.

Also visible in Fig. 3 is a narrow γ-ray peak appearing earlier in time than the neutrons. This peak is called the γ flash, and physically corresponds to beam γ rays that scattered off of the target and interacted in the detector. The time of the γ flash was used to determine the detected neutron energies. There is a small change in the γ flash at low values of PSD. This walk was eliminated by removing the hardware PSD threshold of

the MPD-4 module and increasing the PH threshold during runs dedicated to measuring the position of the γ flash.

The energy of the detected neutrons could be determined from their time of flight by measuring the distance from the target to the detector and using the time of the γ flash. The monoenergetic neutrons from the D_2O measurement were used to make slight adjustments to the distance to correct for the finite thickness of the active volume of the detectors. The energy resolution of the detector system is 180 keV for 2 MeV neutrons and 900 keV for 9 MeV neutrons.

The prompt neutron energy spectrum was divided into eight consecutive 1-MeV wide bins starting at $E_n = 1.5$ MeV. Data uncorrelated with a γ-ray beam pulse were measured using out-of-time cuts and used to subtract background events. The spectrum was then corrected for the detection efficiency bin-by-bin using previously measured detector efficiencies [49,50]. Finally, the instrumental asymmetry corrections were applied by normalizing the yield in each neutron energy bin to the yield in that bin when using a circularly polarized beam. This procedure corrected for differences in solid angle, detection efficiency, and software cut efficiencies between detectors. The average magnitude of these corrections was ~9% and the average uncertainty on the correction was ~2%.

Sample neutron spectra after these corrections were applied are shown in Fig. 4. Significant asymmetries are seen between the yields in the plane of beam polarization ($\phi = 0°, 180°$) and perpendicular to the plane of beam polarization ($\phi = 90°, 270°$). These neutron yields were used to calculate Σ using Eq. (3). Section V shows the results of investigating Σ as a function of scattering angle θ, the beam energy E_γ, and the neutron energy E_n.

The measured values of $\Sigma(\theta)$ were fit using Eq. (4) to extract values of the b and c coefficients for each target and beam energy combination. These values were corrected for the finite size of the detectors using a GEANT4 Monte Carlo simulation [51], which typically increased the values of the coefficients by approximately 4%. The b and c coefficients were also corrected for the presence of contaminant isotopes in each target.
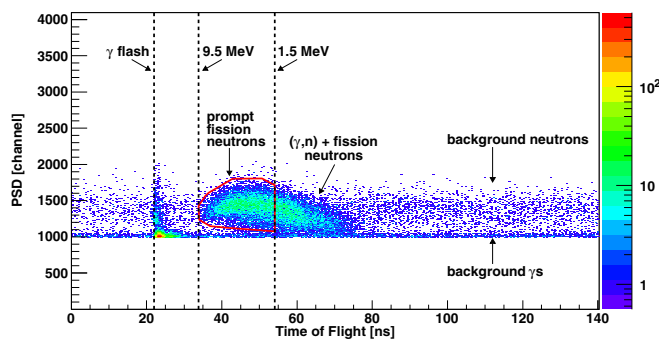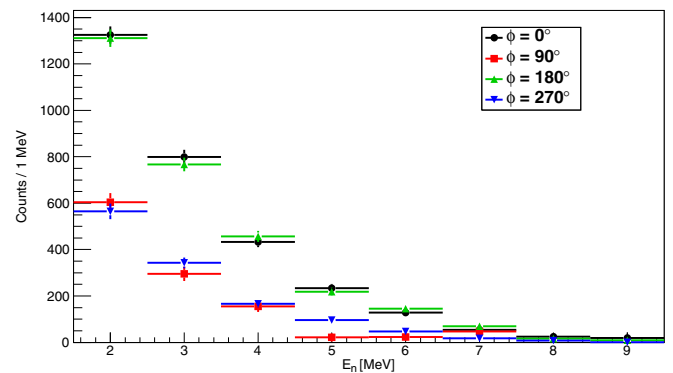

FIG. 3. (Color online) A typical two-dimensional TOF vs PSD spectrum for prompt neutrons from photofission. Data shown are from ^{239}Pu at a beam energy of 7 MeV and a scattering angle of 90°. The red cut indicates the prompt neutrons.

FIG. 4. (Color online) Prompt neutron energy spectra at $\theta = 90°$, parallel and perpendicular to the plane of beam polarization, are shown for photofission of ^{238}U at a beam energy of 5.8 MeV.

Systematic uncertainties

The systematic uncertainties due to the instrumental asymmetries, selection of the cut windows, and possible gain shifts were evaluated. The dominant systematic uncertainty arose from the statistical uncertainty on the circularly polarized beam measurements of instrumental asymmetries ($\sim$2%). This uncertainty was not correlated between detectors at different scattering angles or measurements at different neutron energies, but it was correlated for measurements at different beam energies; at each beam energy, the same measurement with a circularly polarized beam was used to correct for instrumental asymmetries. Each target had its own instrumental correction with a circularly polarized beam, so the systematic uncertainty was not correlated between different targets.

A smaller systematic uncertainty arose from the selection of the cut window, as shown in Fig. 3. This cut was optimized by adjusting its vertical placement and size to minimize the relative uncertainty in the background-subtracted yield. The systematic uncertainty due to the placement of the cut was measured by slightly adjusting the cut. In general, the cut placement had only small uncertainties, since the instrumental asymmetry corrections were recalculated after each cut adjustment, and these corrections account for the cut efficiency. This systematic uncertainty was typically much smaller than the uncertainty due to the instrumental asymmetry correction.

Finally, systematic uncertainties due to possible gain shifts in the detectors and finite-size effects were examined. These uncertainties were estimated to be on the order or smaller than 0.3%, so they have been neglected.

V. RESULTS

The results of the measurement of $\Sigma(90°)$ as a function of E_γ are shown in Fig. 5. Prompt neutrons from photofission of ^{232}Th, ^{238}U, and ^{240}Pu show large polarization asymmetries especially for the lower beam energies studied. On the other

FIG. 6. (Color online) The measured polarization asymmetry $\Sigma(90°)$ as a function of binned neutron energy E_n using yields integrated over all beam energies less than 6.2 MeV. The unbent (black) error bars indicate statistical uncertainties, and the bent-left (red) error bars indicate systematic uncertainties. The systematic uncertainties are uncorrelated. Uncertainties not shown are smaller than the size of the data points.

hand, the odd-A actinides give rise to very small polarization asymmetries. $\Sigma(90°)$ is mathematically equivalent to b as shown in Eq. (4), so a detailed discussion of these data will be provided accompanying Fig. 8 because the statistical uncertainty on the b coefficient is improved compared to $\Sigma(90°)$, and the b coefficients include all of the finite-size and contamination corrections, while the $\Sigma(90°)$ data do not.

The dependence of $\Sigma(90°)$ on E_n for beam energies below 6.2 MeV is shown in Fig. 6. For ^{232}Th and ^{238}U, $\Sigma(90°)$ increases with increasing neutron energy. ^{240}Pu also shows an increasing asymmetry with increasing neutron energy until approximately $E_n = 6$ MeV, where the asymmetry declines, though the highest energy points have large uncertainties. For the odd-A targets, no such correlation between the asymmetry and neutron energy is observed.

In addition to the measurements of $\Sigma(90°)$ as a function of beam energy and neutron energy, $\Sigma(\theta)$ was fit as a function of θ to determine the b and c coefficients in Eq. (4). A typical fit is shown in Fig. 7. The average χ^2 per degree of freedom for these fits is about 1.2.

Figure 8 shows the extracted b coefficients as a function of beam energy, and Fig. 9 shows the extracted c coefficients. These coefficients have been corrected for finite size effects and the presence of contaminant isotopes in each target.

The data in Fig. 8 generally show the same behavior for b as that of $\Sigma(90°)$ in Fig. 5, except with reduced error bars owing to the better statistics obtained by including additional detectors in the fit. The even-even isotopes all have relatively large values of the b coefficient. The differences between the results for these isotopes could be related to the heights of their outer fission barriers, or in the case of a triple-humped barrier, the larger of the two outermost barriers. In the double-humped barrier model, empirical values of the outer barrier height are 6.70, 5.50, and 5.15 MeV for ^{232}Th, ^{238}U, and ^{240}Pu respectively [52]. When the b coefficients are plotted as a function of the difference between the beam energy and the outer fission barrier height, the results for these three isotopes
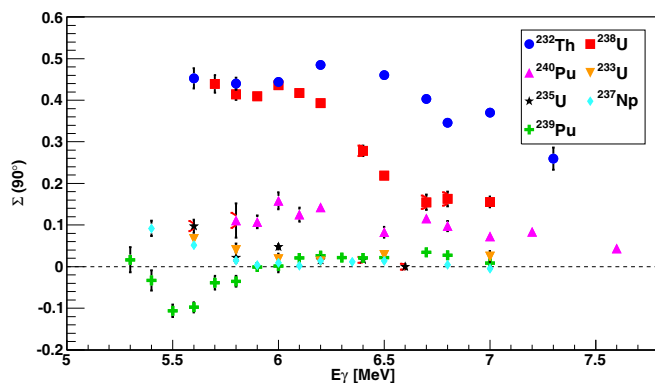

FIG. 5. (Color online) The measured polarization asymmetry $\Sigma(90°)$ as a function of beam energy E_γ using yields integrated over all neutron energies between 1.5 and 9.5 MeV. The unbent (black) error bars indicate statistical uncertainties, and the bent-left (red) error bars indicate systematic uncertainties. The systematic uncertainties are correlated only between points of the same target. Uncertainties not shown are smaller than the size of the data points.
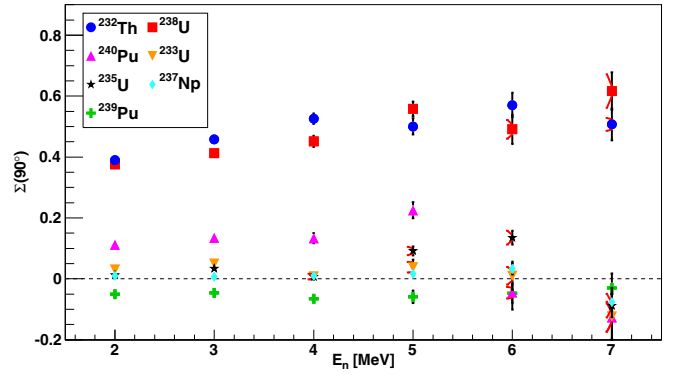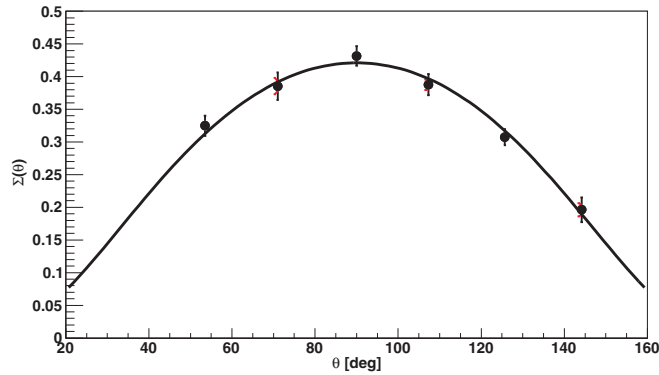
FIG. 7. (Color online) The measured polarization asymmetry $\Sigma(\theta)$ using yields integrated over all neutron energies between 1.5 and 9.5 MeV. The data shown are from photofission of ^{238}U at 5.8 MeV. The unbent (black) error bars indicate statistical uncertainties, and the bent-left (red) error bars indicate systematic uncertainties. The systematic uncertainties are uncorrelated. Uncertainties not shown are smaller than the size of the data points. The best fit parameters using Eq. (4) are $b = 0.433 \pm 0.011 \pm 0.006$ and $c = -0.012 \pm .017 \pm 0.009$, where the first uncertainties are statistical and the second are systematic.

are more similar, though better agreement is achieved with a barrier height of 5.80 MeV for ^{238}U. For the odd-A actinides, statistically significant non-zero b coefficients are observed for beam energies less than 6 MeV. Values of b consistent with 0 are observed for photofission of ^{233}U and ^{235}U at and above 6 MeV, while ^{237}Np and ^{239}Pu both show statistically significant nonzero b values in this region. The difference in ground-state spin between ^{233}U, ^{237}Np, and ^{235}U ($\frac{5}{2}$, $\frac{5}{2}$, and $\frac{7}{2}$) and ^{239}Pu ($\frac{1}{2}$) is probably largely responsible for the observed differences in their measured b values.
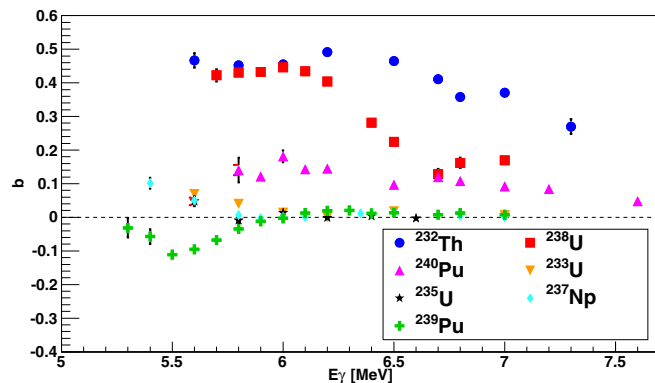

FIG. 8. (Color online) The values for b extracted from the two parameter fits are shown as a function of the beam energy E_γ. Yields were integrated over all neutron energies between 1.5 and 9.5 MeV. The unbent (black) error bars indicate statistical uncertainties, and the bent-left (red) error bars indicate systematic uncertainties. The systematic uncertainties are correlated only between points of the same target. Uncertainties not shown are smaller than the size of the data points.
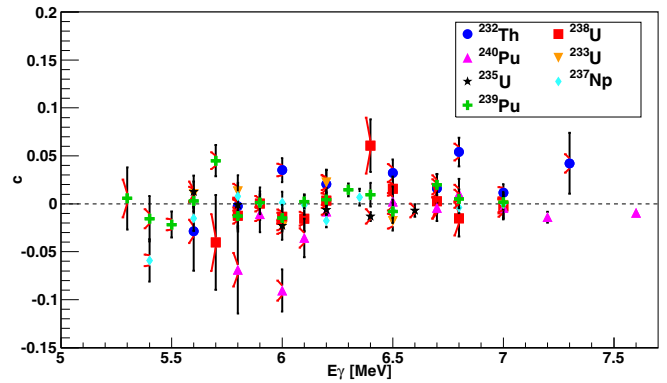

FIG. 9. (Color online) The values for c extracted from the two parameter fits are shown as a function of the beam energy E_γ. Yields were integrated over all neutron energies between 1.5 and 9.5 MeV. The unbent (black) error bars indicate statistical uncertainties, and the bent-left (red) error bars indicate systematic uncertainties. The systematic uncertainties are correlated only between points of the same target. Uncertainties not shown are smaller than the size of the data points.

Figure 9 shows the extracted c values as a function of the beam energy. All of the isotopes are consistent with a c value of 0 except for ^{240}Pu.

VI. CALCULATION

A calculation was performed to predict the values of $\Sigma(90^\circ)$, b, and c. The primary ingredient in this calculation is the code FREYA [53–57]. FREYA is an event-by-event Monte Carlo prompt neutron + γ-ray emission calculation, which simulates the fission process using a few parameters specifically tuned to improve the agreement with available experimental data. It was designed primarily for use in neutron-induced and spontaneous fission. For the present work, it was adapted for use in photofission of ^{238}U and ^{240}Pu. A full description of FREYA is given in Refs. [53–57], but a brief description is provided here.

FREYA begins by partitioning the mass and charge between the two fission fragments. At these energies, only first-chance fission is possible. The fragment masses for photofission of ^{238}U were interpolated directly from experimentally measured masses using 500-keV neutron-induced fission [58], while for ^{240}Pu a five-Gaussian fit was performed to the measured masses for neutron-induced fission of ^{239}Pu [56] and this fit was used to select the fragment masses. The fragment charges were then selected from a Gaussian distribution with a width extracted from data [59]. Next, the average total kinetic energy was taken from measured values of $\overline{\mathrm{TKE}}(A)$ from an average of Refs. [60–62] for ^{240}Pu and from Ref. [63] for ^{238}U. A small adjustment to the average total kinetic energy was made in order to ensure good agreement between predicted and measured average prompt neutron multiplicities. Then, the average total excitation energy was obtained as the difference between the Q value for the reaction and the average total kinetic energy. The Q value was calculated using masses from Ref. [64], supplemented by Ref. [65]

when necessary. The average total excitation energy was first partitioned to the two fragments by assuming they have the same temperature. This was further adjusted by giving the light fission fragment 10% more energy for ^{240}Pu and 20% more energy for ^{238}U to improve the agreement with the experimentally observed prompt neutron multiplicity as a function of fragment mass [56]. The heavy fragment excitation energy was reduced by a corresponding amount. Finally, the excitation energies of the fragments were allowed to thermally fluctuate on an event-by-event basis, and the total kinetic energy was adjusted to conserve energy overall in each fission event.

After the fragments were generated, each fragment was assumed to decay by sequential prompt neutron emission until it was no longer energetically possible. It was assumed that the fragments have fully accelerated before the prompt neutrons were emitted. The prompt neutrons were emitted with no preferred direction in the rest frame of each fragment, and the neutron energy was chosen from an evaporation spectrum: $P(\epsilon) \propto \epsilon e^{-\beta\epsilon}$, where ϵ is the neutron energy in the rest frame of the fragment, and β is the inverse of the temperature of the fragment. The neutrons were then boosted into the laboratory frame.

Direct photofission calculations using FREYA were performed at three beam energies for ^{238}U (5, 6, and 7 MeV) and two energies for ^{240}Pu (5 and 7 MeV). For the results presented as a function of beam energy, the FREYA data set used was a linear combination of the two nearest energy data sets.

In the calculation, the fragment momentum direction was fixed to be along the z axis. The fragment angular distribution when using a linearly polarized beam was calculated from the previously measured reconstructed fragment angular distribution from Ref. [2], adapted for a linearly polarized beam using the procedure in Ref. [35]. Then, each event (fragments + neutrons) was rotated by a random θ and ϕ selected from this calculated fragment angular distribution. Note that the fragment angular distribution was assumed to be
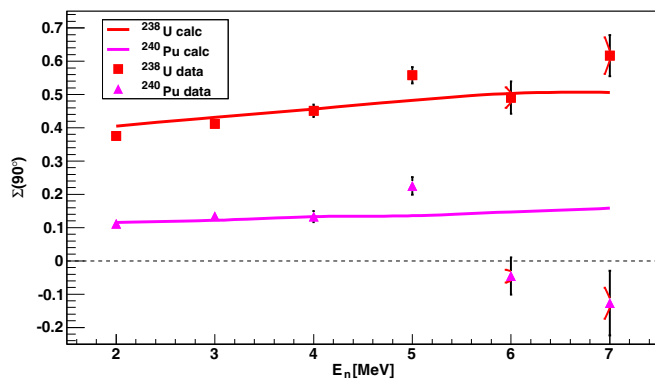

FIG. 11. (Color online) The measured b values for ^{238}U and ^{240}Pu as a function of beam energy E_γ are compared to the results of the calculation. Yields were integrated over all neutron energies between 1.5 and 9.5 MeV. The unbent (black) error bars indicate statistical uncertainties, and the bent-left (red) error bars indicate systematic uncertainties. The systematic uncertainties are correlated only between points of the same target. Uncertainties not shown are smaller than the size of the data points.

decoupled from the fragment mass and energy distributions. This assumption has been violated to some extent by the results of previous measurements (see Ref. [24]), but it was required due to a lack of high-precision data. The resulting neutron polarization asymmetries after the event-by-event rotation were calculated as a function of neutron energy, and the prompt neutron angular distribution coefficients b and c were calculated as a function of beam energy.

The prediction for the neutron polarization asymmetry as a function of the neutron energy is shown in Fig. 10. The calculation predicts an increase in the asymmetry with increasing neutron energy, in agreement with the experimental data on ^{238}U. This correlation is physically intuitive; prompt

FIG. 10. (Color online) The measurements of $\Sigma(90°)$ as a function of binned neutron energy E_n for $E_\gamma < 6.2$ MeV are compared to the results of the calculation. The unbent (black) error bars indicate statistical uncertainties, and the bent-left (red) error bars indicate systematic uncertainties. The systematic uncertainties are uncorrelated. Uncertainties not shown are smaller than the size of the data points.
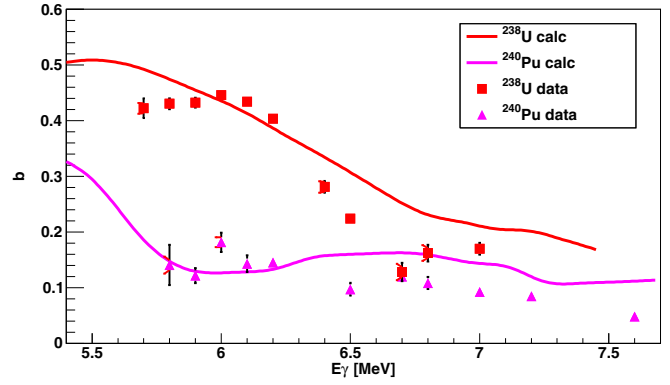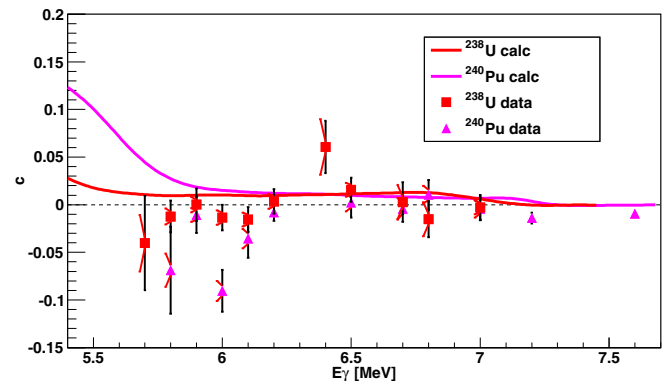

FIG. 12. (Color online) The measured c values for ^{238}U and ^{240}Pu as a function of beam energy E_γ are compared to the results of the calculation. Yields were integrated over all neutron energies between 1.5 and 9.5 MeV. The unbent (black) error bars indicate statistical uncertainties, and the bent-left (red) error bars indicate systematic uncertainties. The systematic uncertainties are correlated only between points of the same target. Uncertainties not shown are smaller than the size of the data points.
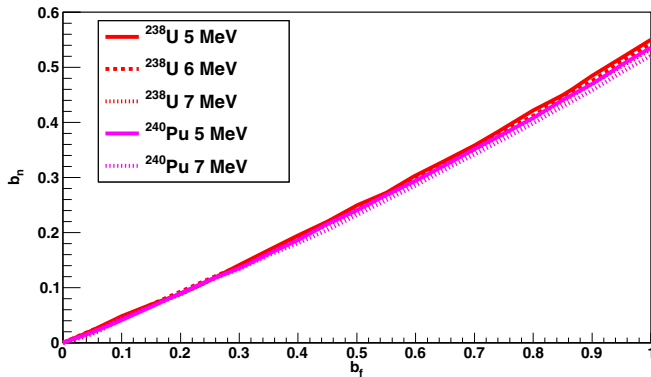
FIG. 13. (Color online) Calculated values of b for the prompt neutrons (b_n) for a given b of the fragments (b_f) are shown for the two different isotopes at different excitation energies. Yields were integrated over all neutron energies between 1.5 and 9.5 MeV.

neutrons that were traveling in the same direction as the fission fragments will gain the most energy when they are boosted into the laboratory frame, and these neutrons tend to become the higher energy neutrons in the laboratory frame. The polarization asymmetries from the fragments are expected to be large (>0.9 for ^{238}U below 6 MeV), so these higher energy neutrons should tend to have larger polarization asymmetries.

The calculated and measured b and c coefficients are compared in Figs. 11 and 12, respectively. Good agreement is found between the scale and trends of the calculation and the measurements of the b coefficient. Particularly good agreement is seen at the lowest beam energies. At these energies, it is expected that the fragment angular distributions are the most accurate, since the reconstruction procedure to unfold the bremsstrahlung beam energy distribution from the measured data in Ref. [2] should have the least uncertainty at the lower energies. The calculated c coefficient is small in accordance with the experimental results.
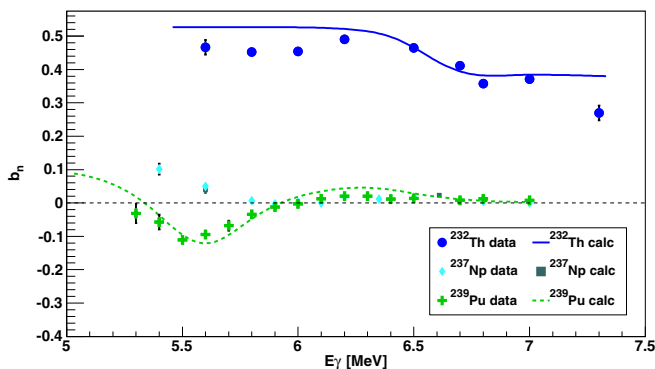

FIG. 14. (Color online) The measured b_n values for ^{232}Th, ^{237}Np, and ^{239}Pu as a function of beam energy E_γ are compared to the results of a calculation using Eq. (5). Yields were integrated over all neutron energies between 1.5 and 9.5 MeV. The unbent (black) error bars indicate statistical uncertainties, and the bent-left (red) error bars indicate systematic uncertainties. The systematic uncertainties are correlated only between points of the same target. Uncertainties not shown are smaller than the size of the data points.

The sensitivity of the calculation to the different experimental conditions was also examined. Figure 13 shows the prompt neutron b coefficient (b_n) as a function of the fragment b coefficient (b_f) along with the dependence on target and beam energy. The value of b_n predicted by the simulation seems to depend much more strongly on b_f than on the target or the beam energy. A general relationship between b_n and b_f was extracted for all neutrons greater than 1.5 MeV from this simulated data:

$$b_n = 0.423b_f + 0.111b_f^2 \tag{5}$$

Equation (5) was used to predict the values of b_n for three targets for which a direct FREYA simulation was not performed due to a lack of experimental data: ^{232}Th, ^{237}Np, and ^{239}Pu. The values for b_f as a function of beam energy were taken from Refs. [2], [4], and [3] for ^{232}Th, ^{237}Np, and ^{239}Pu, respectively. Figure 14 shows the predicted values of b_n compared to the experimental results. Good agreement is again found, particularly in the case of ^{239}Pu.

VII. CONCLUSIONS AND FUTURE WORK

High-precision measurements of prompt neutron polarization asymmetries in photofission of ^{232}Th, ^{233,235,238}U, ^{237}Np, and ^{239,240}Pu have been performed at the HIγS facility. The prompt neutrons from photofission of the even-even actinides exhibit large polarization asymmetries ($\sim$0.5), while those from photofission of the odd-A actinides show little to no polarization asymmetries. The differences in asymmetries between the even-even actinides and odd-A actinides are likely due to their different spins and level densities, which for the even-even actinides lead to polarization asymmetries in the fission fragments and corresponding asymmetries in the prompt neutrons. Angular distribution coefficients b and c were extracted and corrected for target-contamination and finite-size effects, yielding high-precision measurements of these coefficients. The values of these coefficients are in good agreement with predictions based on a model composed of state of the art prompt neutron emission calculations (FREYA) and previously measured fragment angular distributions. This model assumes that the prompt neutrons are emitted with no preferred direction in the rest frame of the fragments. The good agreement between the calculated and experimental results suggests that the prompt neutrons may be used as a precise probe of the underlying fragment angular distribution.

Future work will include extending the study to other actinides, including ^{232,236}U and ^{241}Am. High precision measurements of fragment angular distribution coefficients could also be useful for a direct test of Eq. (5). In addition to enhancing the experimental program, further improvements will be made to the simulation to make it more directly applicable to photofission. The dependence of the neutron b coefficient on the fragment c coefficient will also be investigated using the simulation.

ACKNOWLEDGMENTS

[1] R. Vandenbosch and J. R. Huizenga, *Nuclear Fission* (Academic, New York, 1973).

[2] N. S. Rabotnov, G. N. Smirenkin, A. S. Soldatov, L. N. Usachev, S. P. Kapitza, and Yu. M. Tsipenyuk, Sov. J. Nucl. Phys. **11**, 285 (1970).

[3] A. S. Soldatov, Yu. M. Tsipenyuk, and G. N. Smirenkin, Sov. J. Nucl. Phys. **11**, 552 (1970).

[4] L. P. Geraldo, J. Phys. G **12**, 1423 (1986).

[5] V. E. Zhuchko, Yu. B. Ostapenko, G. N. Smirenkin, A. S. Soldatov, and Yu. M. Tsipenyuk, Sov. J. Nucl. Phys. **27**, 746 (1978).

[6] J. M. Mueller *et al.*, Phys. Rev. C **85**, 014605 (2012).

[7] J. M. Mueller, Ph.D. thesis, Duke University, 2013.

[8] A. P. Baerg, R. M. Bartholomew, F. Brown, L. Katz, and S. B. Kowalski, Can. J. Nucl. Phys. **37**, 1418 (1959).

[9] H. G. de Carvalho and A. G. da Silva, Il Nuovo Cimento **19**, 1131 (1961).

[10] B. Forkman and S. A. E. Johansson, Nucl. Phys. **20**, 136 (1960).

[11] A. V. Ignatyuk, N. S. Rabotnov, G. N. Smirenkin, A. S. Soldatov, and Yu. M. Tsipenyuk, Sov. Phys. JETP **34**, 684 (1972).

[12] L. Katz, A. P. Baerg, and F. Brown, in *Proceedings of the Second UN International Conference on the Peaceful Uses of Atomic Energy*, Vol. 15 (United Nations, Geneva, 1958), p. 188.

[13] N. S. Rabotnov *et al.*, in *Proceedings of the Physics and Chemistry of Fission Conference*, Salzburg, 1965 (IAEA, Vienna, 1965), p. 135.

[14] H. G. R. Prakash, G. Sanjeev, K. B. V. Kumar, K. Siddappa, B. K. Nayak, and A. Saxena, Ann. Nucl. Energy **38**, 757 (2011).

[15] H. G. Rajaprakash, G. Sanjeev, K. B. V. Kumar, K. Siddappa, B. K. Nayak, and A. Saxena, Radiat. Meas. **46**, 413 (2011).

[16] V. E. Rudnikov, G. N. Smirenkin, A. S. Soldatov, and S. Juhasz, Sov. J. Nucl. Phys. **48**, 414 (1988).

[17] E. J. Winhold, P. T. Demos, and I. Halpern, Phys. Rev. **87**, 1139 (1952).

[18] E. J. Dowdy and T. L. Krysinski, Nucl. Phys. A **175**, 501 (1971).

[19] A. Manfredini, L. Fiore, C. Ramorino, H. G. de Carvalho, and W. Wölfli, Nucl. Phys. A **123**, 664 (1969).

[20] A. S. Soldatov, Z. A. Aleksandrova, L. D. Gordeeva, and G. N. Smirenkin, Sov. J. Nucl. Phys. **1**, 335 (1965).

[21] V. M. Khvastunov *et al.*, Phys. At. Nuclei **57**, 1858 (1994).

[22] V. M. Khvastunov and V. V. Denyak, Phys. At. Nuclei **64**, 1269 (2001).

[23] R. Ratzek *et al.*, Z. Phys. A **308**, 63 (1982).

[24] F. Steiper, T. Frommhold, W. Henkel, A. Jung, U. Kneissl, and R. Stock, Nucl. Phys. A **563**, 282 (1993).

[25] S. Nair, D. B. Gayther, B. H. Patrick, and E. M. Bowey, J. Phys. G **3**, 965 (1977).

[26] A. Bohr, in *Proceedings of the UN International Conference on the Peaceful Uses of Atomic Energy*, Vol. 2 (United Nations, Geneva, 1956), p. 151.

[27] S. G. Kadmensky, Phys. At. Nuclei **65**, 1390 (2002).

[28] S. G. Kadmensky and L. V. Rodionova, Phys. At. Nuclei **66**, 1219 (2003).

[29] S. G. Kadmensky and L. V. Titova, Bull. Russ. Acad. Sci. Phys. **72**, 324 (2008).

[30] J. J. Griffin, Phys. Rev. **116**, 107 (1959).

[31] G. Racah, Phys. Rev. **84**, 910 (1951).

[32] U. Fano, Phys. Rev. **90**, 577 (1953).

[33] L. Biedenharn and M. Rose, Rev. Mod. Phys. **25**, 729 (1953).

[34] G. R. Satchler, Proc. Phys. Soc. A **68**, 1041 (1955).

[35] L. W. Fagg and S. S. Hanna, Rev. Mod. Phys. **31**, 711 (1959).

[36] H. R. Weller *et al.*, At. Data Nucl. Data Tables **50**, 29 (1992).

[37] A. S. Vorobyev *et al.*, Nucl. Instrum. Methods A **598**, 795 (2009).

[38] G. R. Keepin, T. F. Wimett, and R. K. Zeigler, J. Nucl. Energy **6**, 1 (1957).

[39] J. S. Fraser, Phys. Rev. **88**, 536 (1952).

[40] J. Terrell, Phys. Rev. **113**, 527 (1959).

[41] A. Gavron, Phys. Rev. C **13**, 2562 (1976).

[42] S. G. Kadmensky and D. E. Lyubashevsky, Bull. Russ. Acad. Sci. Phys. **76**, 457 (2012).

[43] V. N. Litvinenko *et al.*, Phys. Rev. Lett. **78**, 4569 (1997).

[44] H. R. Weller *et al.*, Prog. Part. Nucl. Phys. **62**, 257 (2009).

[45] A. M. Bernstein, M. W. Ahmed, S. Stave, Y. Wu, and H. R. Weller, Annu. Rev. Nucl. Part. Sci. **59**, 115 (2009).

[46] R. E. Pywell, O. Mavrichi, W. A. Wurtz, and R. Wilson, Nucl. Instrum. Methods A **606**, 517 (2009).

[47] G. A. Warren (private communication).

[48] A. Ruben *et al.*, in *IEEE Nuclear Science Symposium Conference Record* (IEEE, Piscataway, NJ, 2007), p. 681.

[49] B. A. Perdue, Ph.D. thesis, Duke University, 2010.

[50] D. E. G. Trotter *et al.*, Nucl. Instrum. Methods A **599**, 234 (2009).

[51] J. Allison *et al.*, IEEE Trans. Nucl. Sci. **53**, 270 (2006).

[52] R. Capote *et al.*, Nucl. Data Sheets **110**, 3107 (2009).

[53] J. Randrup and R. Vogt, Phys. Rev. C **80**, 024601 (2009).

[54] R. Vogt, J. Randrup, J. Pruet, and W. Younes, Phys. Rev. C **80**, 044611 (2009).

[55] R. Vogt and J. Randrup, Phys. Rev. C **84**, 044621 (2011).

[56] R. Vogt, J. Randrup, D. A. Brown, M. A. Descalle, and W. E. Ormand, Phys. Rev. C **85**, 024608 (2012).

[57] R. Vogt and J. Randrup, Phys. Rev. C **87**, 044602 (2013).

[58] T. R. England and B. F. Rider, LANL Report no. LA-UR-94-3106, extracted from ENDF, 1994, http://ie.lbl.gov/fission/endf349.pdf.

[59] W. Reisdorf, J. Unik, H. Griffin, and L. Glendenin, Nucl. Phys. A **177**, 337 (1971).

[60] C. Wagemans, E. Allaert, A. Deruytter, R. Barthélémy, and P. Schillebeeckx, Phys. Rev. C **30**, 218 (1984).

[61] C. Tsuchiya *et al.*, J. Nucl. Sci. Technol. **37**, 941 (2000).

[62] K. Nishio, Y. Nakagome, I. Kanno, and I. Kimura, J. Nucl. Sci. Technol. **32**, 404 (1995).

[63] F. Vivès, F.-J. Hambsch, H. Bax, and S. Oberstedt, Nucl. Phys. A **662**, 63 (2000).

[64] G. Audi and A. Wapstra, Nucl. Phys. A **595**, 409 (1995).

[65] P. Möller, J. R. Nix, W. D. Myers, and W. J. Swiatecki, At. Data and Nucl. Data Tables **59**, 185 (1995).